Highly Flexible Transparent Electrodes Containing Ultrathin Silver for Efficient Polymer Solar Cells

Dhriti Sundar Ghosh, Quan Liu,* Paola Mantilla-Perez, Tong Lai Chen,* Vahagn Mkhitaryan, Minghuang Huang, Sean Garner, Jordi Martorell, and Valerio Pruneri*

Transparent electrodes (TEs) having electrooptical trade-offs better than state-of-the-art indium tin oxide (ITO) are continuously sought as they are essential to enable flexible electronic and optoelectronic devices. In this work, a TiO_2-Ag-ITO (TAI)-based TE is introduced and its use is demonstrated in an inverted polymer solar cell (I-PSCs). Thanks to the favorable nucleation and wetting conditions provided by the TiO_2, the ultrathin silver film percolates and becomes continuous with high smoothness at very low thicknesses (3–4 nm), much lower than those required when it is directly deposited on a plastic or glass substrate. Compared to conventional ITO-TE, the proposed TAI-TE exhibits exceptionally lower electrical sheet resistance (6.2 Ω sq^{-1}), higher optical transmittance, a figure-of-merit two times larger, and mechanical flexibility, the latter confirmed by the fact that the resistance increases only 6.6% after 10^3 tensile bending cycles. The I-PSCs incorporating the TAI-TE show record power conversion efficiency (8.34%), maintained at 96% even after 400 bending cycles.

1. Introduction

Thin films of Ag have been extensively employed in a variety of applications including plasmonics, optical metamaterials, and low-emissivity coatings.[1–3] Another important application of Ag films, in their ultrathin form (thickness < 10 nm), is transparent electrodes (TEs), which are essential materials in many optoelectronic and photonic devices. For example, in solar cells the TE's transparency permits the light to reach the active layers while their conductivity to collect the generated electrical charges.[4,5] Due to its highest conductivity among metals (1.62×10^{-8} Ω m) and low optical loss in the visible spectrum (refractive index ≈ 0.1), Ag is an ideal material for TEs. In order to improve further the optical transmission of Ag films one can suppress the residual reflections by applying proper undercoat and overcoat layers, typically made of transparent oxides, and achieving in this way oxide–metal–oxide (OMO) structures. The OMO multilayer structure has also the advantage to protect the Ag film from oxidation in the operating environment and from chemical reactions that might arise when in contact with other device layers.[6,7] The electrooptical performances of OMO-TEs are highly related to the inverse relationship existing between electrical conductance and optical transmission. With the metal thickness increasing, the electrical conductance increases while the optical transmission decreases.[8,9] In addition to increased absorption, a too thick Ag layer would result in strong reflection of visible light, which cannot be efficiently suppressed by the OMO dielectric layers.

It is known that Ag films deposited by physical vapor deposition techniques tend to grow with island-like mode (Volmer–Weber growth mode), consequently exhibit a rough surface morphology with large grain size and high electrical resistivity, which severely affect the performance of devices.[10–12] Typically, the optimum thickness for ultrathin metals, including Ag films, lies near their percolation, which is defined as the thickness corresponding to which metal islands start to colligate and form a continuous film, resulting in macroscopic electrical conduction.[13,14] Nucleation and wettability are crucial to reduce percolation thickness and increase continuity of the films. Significant research has been carried out to use high energy seed layers,[15–17] self-assembled monolayers (SAMs),[18,19] controlled substrate temperature,[20] cosputtering Al,[21] or oxygen doping[22] to facilitate the uniform and continuous growth of Ag films.

Another crucial aspect of OMO-TEs is the choice of the top oxide layer that, besides the appropriate refractive index and thickness to provide antireflection properties, has to be

Dr. D. S. Ghosh, Q. Liu, P. Mantilla-Perez, Dr. T. L. Chen, V. Mkhitaryan, Prof. J. Martorell, Prof. V. Pruneri
ICFO-Institut de Ciencies Fotoniques
The Barcelona Institute of Science and Technology
08860 Castelldefels, Barcelona, Spain
E-mail: dhriti.ghosh@icfo.es; quan.liu@icfo.es; tonglai.chen@icfo.es
Dr. M. Huang, Dr. S. Garner
Corning Incorporated
Sullivan Park
Corning, NY 14831, USA
Prof. J. Martorell
Departament de Física i Enginyeria Nuclear
Universitat Politècnica de Catalunya
08222 Terrassa, Spain
Prof. V. Pruneri
ICREA- Institució Catalana de Recerca i Estudis Avançats
08010 Barcelona, Spain

DOI: 10.1002/adfm.201503739

compatible and possibly enhance the functionality of other layers forming the device, e.g., the electron transport layer in an inverted polymer solar cell (I-PSC).[23,24] So far, in most of the work carried out on OMO-TEs, the top capping layer is a dielectric oxide of 30–50 nm thickness characterized by high electrical resistivity.[25,26] In fact, such a thickness is too large for efficient charge extraction/collection in a PSC and this often results in lower fill factor (FF) and decreased performance in the PSCs.[27] A top oxide which is conductive would be extremely beneficial for reducing extraction barrier and collection loss of the separated charges.

Here, we report a TE made of ultrathin Ag film (8 nm) in between thin TiO_2 and indium tin oxide (ITO) layers (that we name TiO_2-Ag-ITO (TAI)-TE which shows very low optical loss (average visible transmittance of ≈88%) and extremely low sheet resistance (R_S) (6.2 Ω sq^{-1}). The high refractive index TiO_2 undercoat (bottom) layer facilitates the growth of smooth, highly conductive, and continuous Ag film by sputtering method. The Ag thin film is then capped by a thin ITO layer which ensures both electrical conduction and, together with TiO_2 layer, antireflection effect, permitting a high optical transmittance in the visible spectrum. The thickness of the top capping ITO layer is one third of present state-of-the-art single layer ITO (135 nm) electrode, thus also contributing in reducing the consumption of indium, which is scarce and expensive. PSCs which have shorter energy payback time compared to other photovoltaic technologies were fabricated with the developed TEs.[28] I-PSCs fabricated using TAI-TE show very high performance with photon conversion efficiency (PCE) of 8.34% and enhanced FF (75.7%) for a bulk heterojunction active layer (PTB7:$PC_{71}BM$). The proposed approach can also be applied to plastic substrates, resulting in highly efficient flexible PSCs with superior mechanical properties.

2. Results and Discussion

2.1. Design of TAI Electrodes

Ag thin films are highly prone to oxidation and corrosion, even when exposed to ambient atmosphere. For example they can quickly react with small traces of hydrogen sulfide (H_2S) and oxidize, with detrimental effects on their electrical conductivity and transparency.[29] It has been shown that the chemical stability of Ag thin film greatly improves by embedding them in suitable protective layers, as it is the case of stable ITO in the proposed TAI electrode. To design the TAI electrodes, i.e., to determine the optimum thicknesses of TiO_2 and ITO layers, transfer matrix method (TMM) was utilized.[30,31] The TMM is a mathematical formalism which is based on Fresnel equations that can be efficiently applied to estimate the optical response of the system including the overall transmittance, reflection of the structure, and absorption in each layer. This formalism requires knowledge of the complex refractive index ($\tilde{n}(\lambda) = n(\lambda) + i\kappa(\lambda)$) of the materials. The imaginary part κ (extinction coefficient) is responsible for absorption while the real part n defines the speed of light in the layer. In an ideal case, to maximize the transmittance, besides having low absorption ($\kappa \approx 0$) for both dielectric layers, the bottom layer should have a high n while the capping layer a low n.[25,32]

In the literature, transmittance of a TE can be given at a specific wavelength, λ = 550 nm, or as an average value, $T_{avs} = \int_{\lambda_1}^{\lambda_2} T_\lambda \, d\lambda / \int_{\lambda_1}^{\lambda_2} d\lambda$, over a defined λ_2–λ_1 range.[33,34] To accurately compare transmittance for solar applications, in this work we use the average visible transmittance (375–700 nm), $T_{ave,solar}$, weighted over the air mass (AM) 1.5G solar spectrum:

$$T_{ave,solar} = \frac{\int_{\lambda_1}^{\lambda_2} I_{AM1.5G}(\lambda) T(\lambda) d\lambda}{\int_{\lambda_1}^{\lambda_2} I_{AM1.5G}(\lambda) d\lambda} \quad (1)$$

Figure 1a shows the structure of the TAI-TEs. The $T_{ave,solar}$ was calculated for varying thickness of the bottom TiO_2 and ITO capping layers, between 0 and 100 nm, and a constant Ag thin film thickness of 8 nm. It can be seen in Figure 1b that the effective reflection is strongly dependent on the thicknesses of the TiO_2 and ITO layers and that maximum transmittance can be achieved for ≈30 and ≈45 nm, respectively. The final optimized TAI-TE geometry was TiO_2(30 nm)/Ag(8 nm)/ITO(45 nm). The optimum thicknesses of dielectric layers do not change significantly for different Ag thin film thicknesses (Figure S1, Supporting Information).

Figure 1c shows the wavelength dependent transmission of the TAI-TE corresponding to optimum thicknesses of dielectric layers. For comparison, the transmission of the glass (SiO_2) substrate only, commercial ITO (≈135 nm thick) on glass, only Ag 8 nm thin film on glass and on TiO_2 layer on glass are also shown. Note that for an ITO only TE, the lower the ITO thickness the larger the transparency and the resistance. The transmittance of the TAI electrode is very close to that of the glass substrate. The transmittance of only Ag thin film is comparatively low and is accompanied by a peak in the UV region which corresponds to its characteristic plasma frequency. At longer wavelengths, similar to other metals, its reflection increases. Adding a TiO_2 undercoat layer helps improving the transmittance of Ag thanks to antireflection effect, but the result is still far from the desired performance and that of ITO. Instead, with the ITO top layer the resulting TAI shows transmittance comparable, if not better, to state-of-the-art ITO film. In fact, with TAI configuration and thickness optimization we were able to suppress reflection to values even lower than the blank glass (Figure S2, Supporting Information), thus enhancing the transmittance. For example, the average transmittance between 375 and 700 nm is 87.7% and 85.3% for TAI and ITO, respectively. The large visible transmission of the TE is very advantageous for PSCs, strongly absorbing in this range. The photograph in the inset of Figure 1c also confirms the high transparency of the TAI-TE.

2.2. Electrical, Surface, and Mechanical Properties of TAI

We measured the electrical resistivity for varying thickness of Ag film on fused SiO_2 substrate with and without the undercoat TiO_2 layer (Figure 1d). One can conclude that the TiO_2 layer promoted nucleation and percolation of the Ag films which

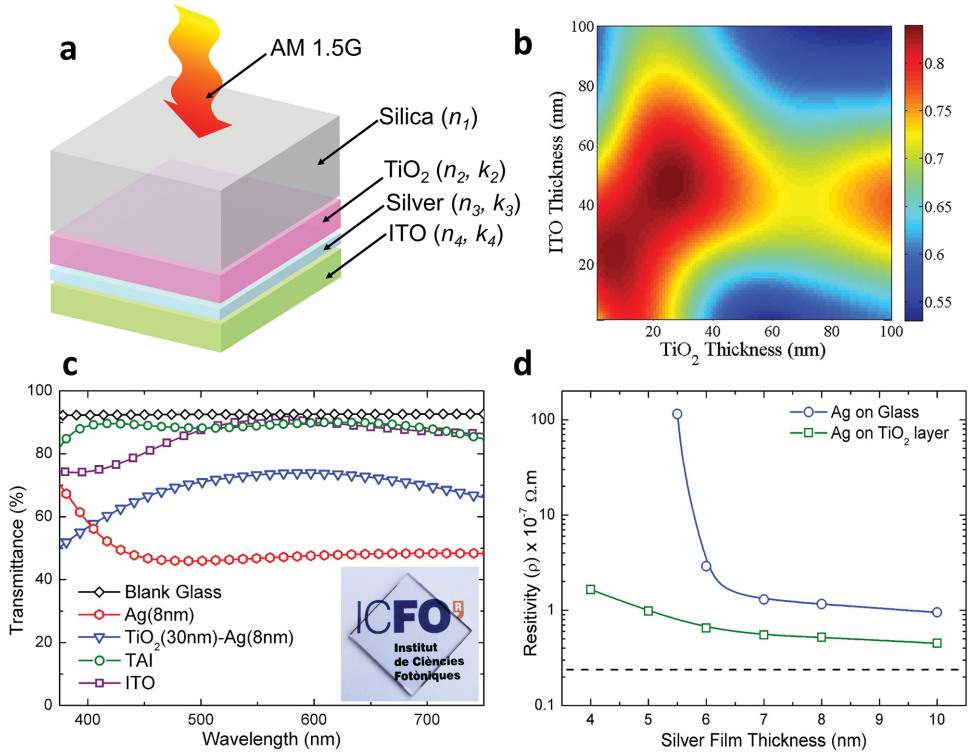

Figure 1. a) Transparent electrode structure studied in this work. b) Simulated average visible (375–700 nm) transmittance of TAI electrode weighted over the AM1.5G solar spectrum for different thicknesses of TiO_2 and ITO for Ag 8 nm film. c) Wavelength dependent optical spectra of the TAI electrode compared to other films and the SiO_2 substrate (the transmission values include the substrate contribution). d) Comparison of electrical resistivity variation for Ag films with and without a bottom TiO_2 seed layer. The dashed line represents the resistivity of bulk Ag film of about 300 nm thickness deposited using the same sputtering process.

show low resistivity even at thickness of 4 nm and below.[35] Whereas the Ag film on glass shows already a dramatic increases of resistivity at 6 nm. Recently, we observed similar phenomena when a thin Cu seed layer was used to promote seeding and percolation.[15] For the TAI electrode to use in the PSC, we chose an Ag film thickness of 8 nm which gives R_S of 6.8 Ω sq^{-1}, further reduced to 6.2 Ω sq^{-1} by the contribution of the 45 nm ITO capping layer.

We also investigated the surface morphology of the deposited film by atomic force microscope (AFM) which confirms the electrical measurement's findings. **Figure 2**a–c shows the AFM height-profile images of Ag 8 nm film deposited on fused SiO_2 substrate, on TiO_2 layer, and also of the overall TAI electrode. The Ag film on fused SiO_2 substrate shows discontinuity characterized by island like structure and large surface roughness (root-mean-square (RMS) roughness of 6.5 nm). In fact, the island like morphology is even clearer in the phase diagram of the film (Figure S3, Supporting Information). Instead, the RMS roughness of the Ag film on TiO_2 layer (2.2 nm) was three times smaller, which clearly indicates improvement in film continuity and uniformity thanks to the undercoat TiO_2 layer. The top ITO layer further smoothens the film (RMS roughness of 0.9 nm).

Another important aspect associated with TEs is their mechanical flexibility, i.e., the retention of electrical properties under multiple bending. The bending test was carried out for TAI films deposited on poly(ethylene terephthalate) (PET) substrate and compared with commercially available thicker

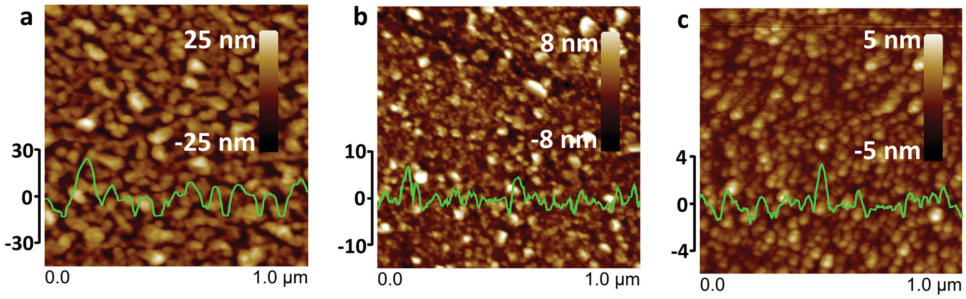

Figure 2. Atomic force microscopy and typical cross section profilometry of a) Ag 8 nm, b) TiO_2 30 nm-Ag 8 nm, and c) TAI-TE.

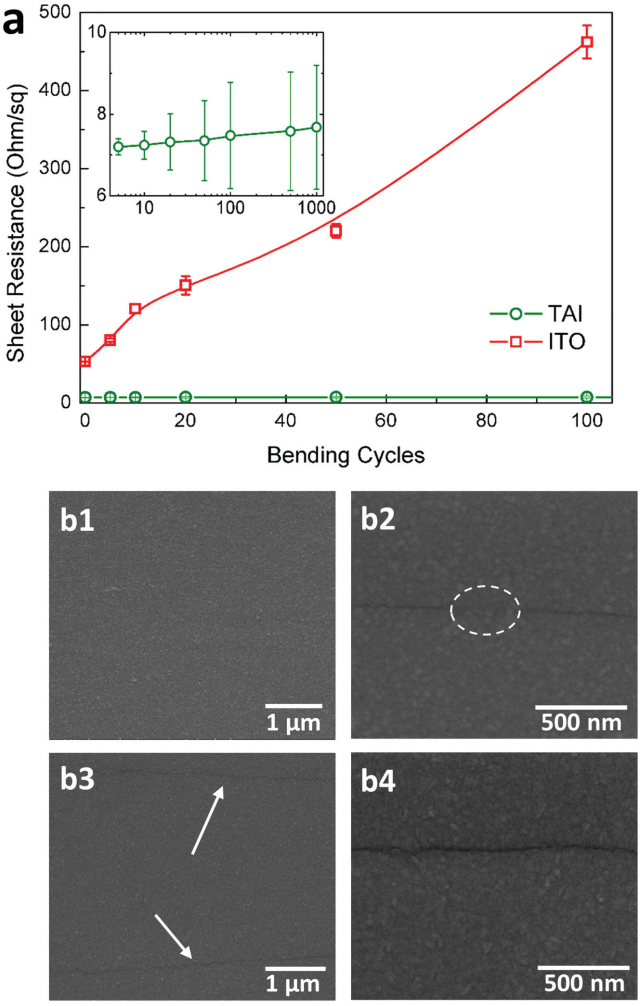

Figure 3. a) Change in R_S after bending as a function of bending cycles for TAI-TEs and conventional ITO-TEs. The inset shows the same for a larger number of bending cycles for TAI-TE. b1–b4) Scanning electron microscope images of b1,b2) TAI and b3,b4) ITO TE films after bending. The dashed oval in (b2) shows an area with continuous film in between a crack while the arrows in (b3) show two crack lines running parallel to the direction of tensile bending.

ITO on PET. The bending radius varied from 10 to 3 mm (Figure S4, Supporting Information) and the electrical R_S was measured as a function of bending cycles. The maximum bending strain (ε_{MAX}) applied was ≈2.1%, calculated using the equation $\varepsilon_{MAX} = h_S/(2R)$, where h_S is the thickness of the PET substrate (125 μm) and R is the minimum bending radius. The results are shown in **Figure 3**a. Thanks to the ductility of the Ag layer, the TAI-TE showed a high degree of flexibility with a small relative increase in R_S of 3.8% and 6.6% after 100 and 1000 bending cycles, respectively, while that of ITO was 128% and 770% after only 10 and 100 cycles, respectively. Figure 3b shows the scanning electron microscope (SEM) images of the TEs after bending test. On a large scale, the TAI film is free of any ruptures (Figure 3b1). However some cracks can be seen on a shorter scale with continuous film patches between them (Figure 3b2), which explains the slight increase in R_S. More and longer cracks can be seen for the ITO film (Figure 3b3) which are also more pronounced and deeper compared to the TAI-TEs (Figure 3b4). Note also that the SEM images for TAI-TE is taken after 1000 cycles while for ITO it is taken after a much smaller number (100) of bending cycles.

The trade-off between R_S and optical transmittance (T) were also compared to other recently published OMO structures, with the TAI-TE showing superior performance. A simple way to compare is using a figure-of-merit (FoM) defined by ratio of DC conductivity and optical conductivity (σ_{DC}/σ_{OP}) which is related to T and R_S: $T = (1+(Z_0/2R_S)(\sigma_{DC}/\sigma_{OP}))^{-2}$ where Z_0 is the free-space impedance.[6,36] High values of σ_{DC}/σ_{OP} indicated high T and low R_S, respectively. TAI-TE exhibits the highest FoM with values close to 500 while ITO reaches 250 (Table S1, Supporting Information).

2.3. I-PSC Performance

To demonstrate the application potential of the highly transparent and low resistance TAI-TE, PSC devices were fabricated with the following structure: Eagle XG Glass/TAI/Sol–gel ZnO (SG-ZnO)/PTB7:$PC_{71}BM$/MoO_3/Ag (**Figure 4**a). This inverted device structure has been shown to have improved ambient stability compared to poly(3,4-ethylenedioxythiophene):poly(styrene sulfonate) (PEDOT:PSS) based direct device structure. The active layer is composed of PTB7:$PC_{71}BM$ bulk heterojunction, which is a well investigated photoactive material, with typical PCE above 7%.[37,39] The reference devices were also fabricated employing standard commercial ITO (135 nm) TE on glass substrate.

Initially we fabricated TAI and ITO-based devices with an active layer thickness of about 90 nm, which was indicated in the literature as the optimal thickness for PTB7:$PC_{71}BM$ structure.[37,40] The current density–voltage (J–V) characteristics of these I-PSCs were measured (Figure 4c) and the parameters-including the short-circuit current density (J_{SC}), open-circuit voltage (V_{OC}), FF, and PCE are summarized in **Table 1**. With 90 nm active layer, the ITO-devices exhibited an average J_{SC} of 15.07 mA cm^{-2}, a V_{OC} of 0.74 V, a FF of 72.4%, and an overall PCE of 8.11%, whereas the TAI-devices exhibited PCE of 7.36% ± 0.10%, with an average J_{SC} of 13.4 mA cm^{-2}, a V_{OC} of 0.74 V, and a FF of 74.4%. Clearly, the performance was reduced in TAI-devices mainly because of lower photocurrent compared to ITO counterparts, which is in good agreement with external quantum efficiency (EQE) measurements, shown in Figure 4d. The EQE spectra for TAI devices with 90 nm thick active layer are lower in intensity than those for the ITO counterparts within the 400–750 nm wavelength range. However, it is worth noting that TAI devices achieved excellent FF with value as high as 75.4%, the highest reported value for the PTB7:$PC_{71}BM$ PSCs. The improved FF in TAI-devices can be attributed to the extremely low R_S of the electrode, which reduces the series resistance of I-PSCs (3.02 Ω cm^2) as compared with ITO devices (5.78 Ω cm^2). Generally, a I-PSC with more transparent TE would yield higher photocurrent, but due to optical interference effect, larger electrode transparency does not imply that the light harvesting in the active layer will be enhanced. To further clarify the interference effect of the TAI electrode on photocurrent generation in the corresponding device, we applied TMM to adequately compare the J_{SC} in terms of SG-ZnO and

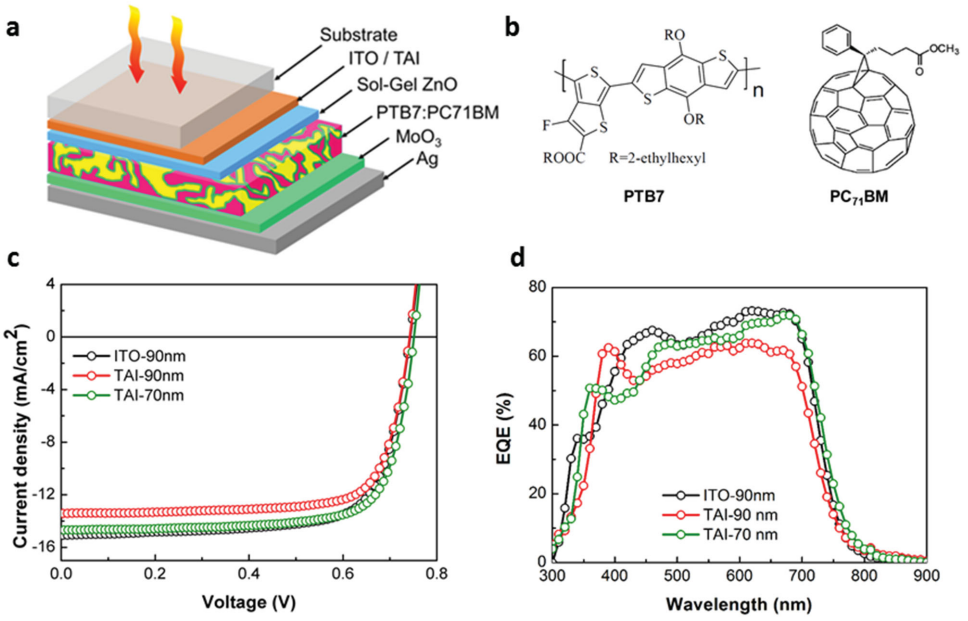

Figure 4. a) Device architecture of I-PSCs. b) Molecular structures of PTB7 and $PC_{71}BM$. c) *J–V* curves of I-PSC under simulated 100 mW cm^{-2} AM1.5G illumination. The values indicate active layer thickness. d) EQE spectra of best-performing I-PSCs.

active layer thicknesses for both cases, shown in **Figure 5**. The optical constants for calculation were taken from literature and details of the model used can be found in ref. [41]. We observed that the calculated photocurrent in TAI or ITO-based I-PSCs is weakly dependent to the thickness of the SG-ZnO for all given active layer's thicknesses and 20 nm thick SG-ZnO offers the best device performance, both theoretically and experimentally. The maximum predicted J_{SC} of ≈15 mA cm^{-2} can be found in the ITO-based device when the active layer's thickness is ≈90 nm, which is consistent with earlier reports.[42] In contrast to ITO, J_{SC} in the TAI device reaches the local maximum when the active layer thickness is reduced to 70 nm while an increase in the active layer thickness from 70 to 120 nm produces a steady decrease in J_{SC}. Following theoretical predictions, a series of TAI-based devices with ≈70 nm thick active layer were fabricated and showed average J_{SC} of 14.61 mA cm^{-2}, V_{OC} of 0.75 V, FF of 74.6%, and PCE of 8.19%, and the best performance was 8.34%, which is even a little better than the best ITO-based device with a PCE of 8.15%. This is among the best reported efficiencies using the ITO/SG-ZnO standard configuration without any additional interfacial modifier, such as poly[(9,9-bis(3'-(N,N-dimethylamino) propyl)-2,7-fluorene)-alt-2,7-(9,9–dioctylfluorene)] (PFN)[43] and poly(ethyleneimine) (PEI).[44] It should be noted that the best FF approaches 76%, which is among the best reported in PSCs and comparable with values obtained in inorganic solar cells.

The opposite J_{SC} variation in TAI-based device is also confirmed by the experimental EQE, which shows spectral enhancement from 450 to 750 nm for TAI-device with 70 nm active layer compared to the 90 nm counterpart. This enhancement can be attributed to absorption improvement by the optical microcavity generated between the thin Ag TAI layer and thick Ag electrodes. Because of the enhanced optical electric field, the optical absorption of the thin active layer is increased, this resulting in EQE enhancement and significant J_{SC} improvement in J_{SC}.[45] Therefore, in PSCs incorporating TAI-TE, it is crucial to tune the active layer thickness within the microcavity to achieve maximum performance.

We also fabricated I-PSCs incorporating the TAI-TE on flexible Corning Willow Glass substrates and evaluated their mechanical flexibility. General properties of flexible glass substrate have been reported previously.[46] Previous reports of flexible glass photovoltaic devices have included copper zinc tin sulfide (CZTS)[47,48] and CdTe structures.[49,50] The photovoltaic parameters were measured as a function of

Table 1. Photovoltaic performance comparison of PTB7:$PC_{71}BM$ solar cells on standard ITO/glass and TAI/glass substrates.

Substrate	J_{SC} [mA cm^{-2}]	V_{OC} [V]	FF [%]	PCE [%]	J_{SC} (EQE)[a] [mA cm^{-2}]	R_{Series} [Ω cm^2]
Standard ITO/glass	15.07 (15.07 ± 0.11)[b]	0.74 (0.74)	72.8 (72.4 ± 0.4)	8.15 (8.11 ± 0.04)	15.32	5.78
TAI/glass[c]	13.44 (13.39 ± 0.08)	0.74 (0.74)	75.4 (74.4 ± 0.6)	7.52 (7.36 ± 0.10)	13.42	3.02
TAI/glass[d]	14.66 (14.61 ± 0.09)	0.75 (0.75)	75.7 (74.6 ± 0.6)	8.34 (8.19 ± 0.11)	14.94	2.67
TAI/Corning Willow Glass[d]	14.33 (14.35 ± 0.19)	0.75 (0.75)	75.8 (74.9 ± 0.6)	8.06 (7.96 ± 0.13)	14.53	2.97

[a]Calculated from the EQE spectra; [b]Average values and standard deviation of device statistics from over six devices are given in parentheses; [c]Nonoptimized device (active layer thickness = 90 nm); [d]Optimized device (active layer thickness = 70 nm).

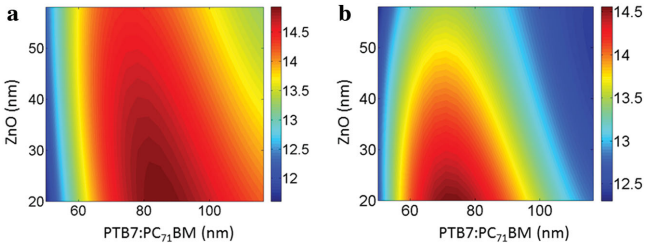

Figure 5. Contour plot of the numerically calculated J_{SC} as a function of the sol–gel ZnO and active layer thickness. a) ITO-based device. b) TAI-based device.

bending radius of curvature and number of cycles, as previously reported.[34] **Figure 6**a,b shows the parameters with respect to the flat geometry for different radii of curvature. Without any bending stress, devices on Willow Glass exhibited similar performance as their nonflexible glass counterparts, with average J_{SC} of 14.34 mA cm^{-2}, V_{OC} of 0.75 V, FF of 75.3%, and PCE of 7.98%. When the bending radius is decreased from 5.4 to 2.2 cm, all the parameters remain stable, always above 98% of the flat geometry values. Finally, performances in terms of the number of bending cycles were also measured with the same device and the stability evolution is shown in Figure 6c,d. V_{OC} and J_{SC} remain almost unchanged with only slightly decrease of 1%, while a very small reduction in FF indicates slight increase in electrical R_S of the TAI electrode under continuous bending. It has to be noted that different bending radii and bending cycles cases, the FF is the parameter mostly affected by the bending stress which results in PCE showing a trend similar to FF. Overall, even after 400 bending cycles the I-PSC on flexible glass retained 96% of its initial value.

3. Conclusion

We proposed and developed TiO_2/Ag/ITO-based transparent electrodes with sheet resistance of 6.2 Ω sq^{-1} and average optical transmittance of 87.6% between 375 and 700 nm. The developed electrode shows only 6.6% increase in resistance after 10^3 tensile bending cycles. These performances, especially in terms of electrical conductance and mechanical flexibility, are much better than state-of-the-art single layer ITO. Crucially to achieve such performance, the bottom TiO_2 layer promotes a continuous and smooth Ag film while the top ITO film forms a conductive capping layer which together with TiO_2 layer creates an antireflection structure. Optimized inverted polymer solar cells, with thin active layer for enhanced absorption, employing such TAI electrodes achieve 8.34% efficiency, higher than similar structures built on conventional ITO substrates. No significant change in solar cell parameters was observed under repetitive bending cycles, demonstrating the mechanical robustness of the approach also at device level. The work shows that the proposed TAI transparent electrodes can effectively be used for flexible and efficient organic optoelectronic devices.

4. Experimental Section

TAI Deposition and Characterization: Double side optically polished UV fused silica/Eagle XG glass substrates, 1 mm thick and 1 inch square was used as substrate. For mechanical flexibility measurements of I-PSCs, Willow Glass (0.140 mm thick and 2 inch by 3 inch) was used. Before TE deposition, the substrates were cleaned in acetone followed by ethanol in ultrasonic bath, each process lasting 10 min. The substrates were then rinsed in abundant deionized (DI) water and dried with nitrogen gas followed by low power argon plasma cleaning for 10 min inside the sputtering machine. The entire TE structure was prepared by magnetron sputtering without breaking the vacuum. The sputtering chamber was

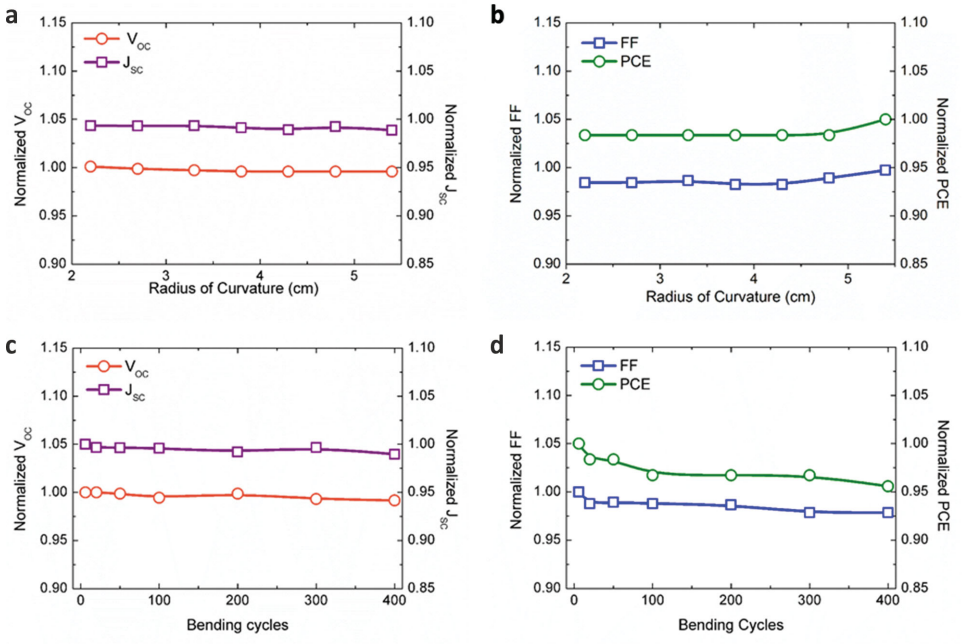

Figure 6. Different solar cell parameters as a function of a,b) radius of curvature and c,d) bending cycles. For (a,b) the *J–V* curves were obtained in situ at different radius of curvature while for (c,d) measurements were carried out in flat configuration after bending.

initially evacuated to a base pressure of ≈10^{-7}–10^{-8} Torr. The target-to-substrate distance was maintained at 30 cm. The substrate holder was rotating during deposition with a speed of 60 rpm. Ag and TiO_2 were deposited in pure Ar atmosphere while ITO (In_2O_3/SnO_2, 90/10 wt%) was deposited in a mixture of Ar/O_2 (flux ratio 20:1), all of them at room temperature. An Ag (99.99%) target was used to deposit the Ag films using a DC power of 100 W and a working pressure of 2 mTorr. The TiO_2 film was deposited in radio frequency (RF) power under the same conditions of the Ag film while the ITO film was deposited at DC power of 60 W and the deposition pressure was maintained at 2 mTorr. The deposition rate was 0.1, 2.3, and 0.7 Å s^{-1} for TiO_2, Ag, and ITO, respectively. The TAI electrodes were afterward annealed at 300 °C for 10 min at ambient condition. The electrical properties of the films were measured using four-point probe method with cascade Microtech 44/7 S 2749 probe system connected to a Keithley 2001 multimeter. Typically, six measurements were performed at different positions on the films and mean values were used to calculate the R_S. A Perkin Elmer lambda 950 spectrometer was used for optical transmission measurements. Surface morphology was investigated by a digital instrument D3100 AFM and FEI-scanning electron microscopy (SEM). The AFM image analysis was carried out with Nanoscope 7.30 software.

PSC Materials and Fabrication: The polymer PTB7 and $PC_{71}BM$ (purity > 99%) were purchased from one-material and American Dye Source, respectively, and were used as received. The sol–gel ZnO precursor solutions (0.3 M) were prepared according to the previously reported method:[41,43] zinc acetate dehydrate (Zn $(CH_3COO)_2{\cdot}2H_2O$, Aldrich, 99.9%, 0.5 g) and ethanolamine ($NH_2CH_2CH_2OH$, Aldrich, 99.5%, 0.14 g) were dissolved in 2-methoxyethanol ($CH_3OCH_2CH_2OH$, Aldrich, 99.8%, 7.5 mL). This solution was vigorously stirred at 60 °C for 2 h to complete the hydrolysis reaction in air and then stirred at room temperature for at least 12 h. Solutions of PTB7:$PC_{71}BM$ (1.0:1.5 wt) at a concentration of 10 mg mL^{-1} were prepared in chlorobenzene with the processing additive 1,8-diiodoctane (97%:3% vol). Devices were fabricated by spin-casting ZnO-Precursor on the precleaned ITO (Lumtec, 135 nm, 15 Ω sq^{-1}) or TAI glass substrates and annealing at 180 °C in air for 10 min to form a 20 nm condensed cathode buffer layer. The prepared samples were then transferred into a N_2-filled glove box for spin-casting the active layer with controlled thicknesses, followed by high-vacuum ($<5 \times 10^{-6}$ mbar) drying for 1 h. Finally, MoO_3 (5 nm) and Ag (120 nm) electrodes were sequentially deposited on the active layer through a shadow mask by thermal evaporation ($<5 \times 10^{-6}$ mbar), which defines the active area of 0.096 cm^2. The deposition rate was 0.5 and 1 Å s^{-1} for MoO_3 and Ag, respectively.

PSC Characterization: J–V curves of all devices were measured with a Keithley 2420 source meter and an Abet Sol3A solar simulator (AM1.5G, 100 mW cm^{-2}). The illumination intensity of the light source (Xenon lamp, 300W, USHIO) was accurately calibrated employing a standard Si photodiode detector certificated by ISE Fraunhofer. Spectrally resolved EQEs were measured using a bench top QEX10 measurement system supplied by PV Measurements Inc. For the mechanical flexibility measurements, the *J–V* curves were obtained in situ at different radius of curvature while measurements were made after the specified bending cycles in flat configuration.

Supporting Information

Supporting Information is available from the Wiley Online Library or from the author.

Acknowledgements

The authors acknowledge financial support from the Spanish Ministry of Economy and competitiveness and "Fondo Europeo de Desarrollo Regional" through Grant TEC2013-46168-R and IPT-2012-0986-120000. This project has received funding from the European Union's FP7 research and innovation programme under Grant Agreement No. 604506. T.L.C. acknowledges financial support through a Ramon y Cajal fellowship. Q.L. acknowledges Erasmus Mundus doctorate program Europhotonics (Grant No. 159224-1-2009-1-FR-ERA MUNDUS-EMJD).

Received: September 3, 2015
Revised: September 22, 2015
Published online: November 5, 2015

[1] D. R. Smith, W. J. Padilla, D. C. Vier, S. C. Nemat-Nasser, S. Schultz, *Phys. Rev. Lett.* **2000**, *84*, 4184.
[2] T. J. Yen, W. J. Padilla, N. Fang, D. C. Vier, D. R. Smith, J. B. Pendry, D. N. Basov, X. Zhang, *Science* **2004**, *303*, 1494.
[3] N. Fang, H. Lee, C. Sun, X. Zhang, *Science* **2005**, *308*, 534.
[4] D. S. Ghosh, *Ultrathin Metal Transparent Electrodes for the Optoelectronics Industry*, Springer Theses, Springer, Berlin, Germany **2013**.
[5] D. S Hecht, L. Hu, G. Irvin, *Adv. Mater.* **2011**, *23*, 1482.
[6] D. S. Ghosh, T. L. Chen, N. Formica, J Hwang, I Bruder, V Pruneri, *Sol. Energy Mater. Sol. Cells* **2012**, *107*, 338.
[7] J. Zou, C.-H. Li, C.-Y. Chang, H.-L. Yip, A. K.-Y. Jen, *Adv. Mater.* **2014**, *26*, 3618.
[8] T. Winkler, H. Schmidt, H. Flügge, F. Nikolayzik, I. Baumann, S. Schmale, T. Weimann, P. Hinze, H.-H. Johannes, T. Rabe, S. Hamwi, T. Riedl, W. Kowalsky, *Org. Electron.* **2011**, *12*, 1612.
[9] N. P. Sergeant, A. Hadipour, B. Niesen, D. Cheyna, P. Heremans, P. Peumans, B. P. Rand, *Adv. Mater.* **2012**, *24*, 728.
[10] M. Hu, S. Noda, H. Komiyama, *Surf. Sci.* **2002**, *513*, 530.
[11] D. Gu, C. Zhang, Y.-K. Wu, L. J. Guo, *ACS Nano* **2014**, *8*, 10343.
[12] M. Ohring, *Materials Science of Thin Films*, 2nd ed., Academic Press, San Diego, CA, USA **2002**, p. 386.
[13] L. Martínez, D. S. Ghosh, S. Giurgola, P. Vergani, V. Pruneri, *Opt. Mater.* **2009**, *31*, 1115.
[14] T. L. Chen, D. S. Ghosh, D. Krautz, S. Cheylan, V. Pruneri, *Appl. Phys. Lett.* **2011**, *99*, 093302.
[15] N. Formica, D. S Ghosh, A. Carrilero, T. L. Chen, R. E. Simpson, V. Pruneri, *ACS Appl. Mater. Interfaces* **2013**, *5*, 3048.
[16] S. Schubert, J. Meiss, L. M. Meskamp, K. Leo, *Adv. Energy Mater.* **2013**, *3*, 438.
[17] V. J. Logeeswaran, N. P. Kobayashi, M. S. Islam, W. Wu, P. Chaturvedi, N. Fang, S. Y. Wang, R. S. Williams, *Nano Lett.* **2009**, *9*, 178.
[18] H. M. Stec, R. Williams, T. S. Jones, R. A. Hatton, *Adv. Funct. Mater.* **2011**, *21*, 1709.
[19] A. Kossoy, V. Merk, D. Simakov, K. Leosson, S. Kéna-Cohen, S. A. Maier, *Adv. Opt. Mater.* **2015**, *3*, 1.
[20] S. E. Roark, K. L. Rowlen, *Anal. Chem.* **1994**, *66*, 261.
[21] C. Zhang, D. Zhao, D. Gu, H. Kim, T. Ling, Y.-K. R. Wu, L. J. Guo, *Adv. Mater.* **2014**, *26*, 5696.
[22] W. Wang, M. Song, T.-S. Bae, Y. H. Park, Y.-C. Kang, S.-G. Lee, S.-Y. Kim, D. H. Kim, S. Lee, G. Min, G.-H. Lee, J.-W. Kang, J. Yun, *Adv. Funct. Mater.* **2014**, *24*, 1551.
[23] D. W. Zhao, P. Liu, X. W. Sun, S. T. Tan, L. Ke, A. K. K. Kyaw, *Appl. Phys. Lett.* **2009**, *95*, 153304.
[24] D. W. Zhao, S. T. Tan, L. Ke, P. Liu, A. K. K. Kyaw, X. W. Sun, G. Q. Lo, D. L. Kwong, *Sol. Energy Mater. Sol. Cells* **2010**, *94*, 985.
[25] D. R. Sahu, J.-L. Huang, *Mater. Sci. Eng. B* **2006**, *130*, 295.
[26] K. Jeon, H. Youn, S. Kim, S. Shin, M. Yang, *Nanoscale Res. Lett.* **2012**, *7*, 253.
[27] J. Krantz, M. Richter, S. Spallek, E. Spiecker, C. J. Brabec, *Adv. Funct. Mater.* **2011**, *21*, 4784.
[28] S. B. Darling, F. You, *RSC Adv.* **2013**, *3*, 17633.
[29] J. L. Elechiguerra, L. Larios-Lopez, C. Liu, D. Garcia-Gutierrez, A. Camacho-Bragado, M. J. Yacaman, *Chem. Mater.* **2005**, *17*, 6042.
[30] J. Chilwell, I. Hodgkinson, *J. Opt. Soc. Am. A* **1984**, *1*, 742.

[31] K.-S. Chen, H.-L Yip, J.-F. Salinas, Y.-X. Xu, C.-C. Chueh, A. K.-Y. Jen, *Adv. Mater.* **2014**, *26*, 3349.
[32] K. Hong, J. H. Son, S. Kim, B. H. Koo, J.-L. Lee, *Chem. Commun.* **2012**, *48*, 10606.
[33] V. D. Groep, P. Spinelli, A. Polman, *Nano Lett.* **2012**, *12*, 3138.
[34] A. Bou, P. Torchio, S. Vedraine, D. Barakel, B. Lucas, J.-C. Bernède, P.-Y. Thoulon, M. Ricci, *Sol. Energy Mater. Sol. Cells* **2014**, *125*, 310.
[35] N. Formica, P. Mantilla-Perez, D. S. Ghosh, D. Janner, T. L. Chen, M. Huang, S. Garner, J. Martorell, V. Pruneri, *ACS Appl. Mater. Interfaces* **2015**, *7*, 4541.
[36] L. Hu, D. S. Hecht, G. Gruner, *Nano Lett.* **2004**, *4*, 2513.
[37] A. M. Otero, Q. Liu, P. M. Perez, M. M. Bajo, J. Martorell, *J. Mater. Chem. A* **2015**, *3*, 10681.
[38] Y. Y. Liang, Z. Xu, J. B. Xia, S.-T. Tsai, Y. Wu, G. Li, C. Ray, L. Yu, *Adv. Mater.* **2010**, *22*, E135.
[39] L. Lu, L. Wu, *Adv. Mater.* **2014**, *26*, 4413.
[40] S. Loser, B. Valle, K. A. Luck, C. K. Song, G. Ogien, M. C. Hersam, K. D. Singer, T. J. Marks, *Adv. Energy Mater.* **2014**, *4*, 1301938.
[41] R. Betancur, A. Martinez-Otero, X. Elias, P. Romero-Gomez, S. Colodrero, H. Miguez, J. Martorell, *Sol. Energy Mater. Sol. Cells* **2012**, *104*, 87.
[42] S. Loser, B. Valle, K. A. Luck, C. K. Song, G. Ogien, M. C. Hersam, K. D. Singer, T. J. Marks, *Adv. Energy Mater.* **2014**, *4*, 1301938.
[43] Y.-M. Chang, C.-Y. Leu, *J. Mater. Chem. A* **2013**, *1*, 6446.
[44] S. Woo, W. H. Kim, H. Kim, Y. Yi, H. K. Lyu, Y. Kim. *Adv. Energy Mater.* **2014**, *4*, 1301692
[45] W. Yu, L. Shen, F. Meng, Y. Long, S. Ruan, W. Chen, *Sol. Energy Mater. Sol. Cells* **2012**, *100*, 226.
[46] S. Garner, S. Glaesemann, X. Li, *Appl. Phys. A* **2014**, *116*, 403.
[47] C.-Y. Peng, T. P. Dhakal, S. M. Garner, P. Cimo, S. Lu, C. R. Westgate, *IEEE Trans. Device Mater. Rel.* **2014**, *14*, 121.
[48] C.-Y. Peng, T. P. Dhakal, S. Garner, P. Cimo, S. Lu, C. R. Westgate, *Thin Solid Films* **2014**, *562*, 574.
[49] W. L. Rance, J. M. Burst, D. M. Meysing, C. A. Wolden, M. O. Reese, T. A. Gessert, W. K. Metzger, S. Garner, P. Cimo, T. M. Barnes, *Appl. Phys. Lett.* **2014**, *104*, 143903.
[50] J. M. Burst, W. L. Rance, D. M. Meysing, C. A. Wolden, W. K. Metzger, S. M. Garner, P. Cimo, T. M. Barnes, T. A. Gessert, M. O. Reese, in *IEEE Photovoltaic Specialist Conf.*, IEEE, Piscataway, NJ, USA **2014**, p. 1589.